Acta Oceanol. Sin., 2022, Vol. 41, No. 2, P. 51–64
https://doi.org/10.1007/s13131-021/1857-4
http://www.aosocean.com
E-mail: ocean2@hyxb.org.cn

A new nudging scheme for the current operational climate prediction system of the National Marine Environmental Forecasting Center of China

Xunshu Song[1, 2*], Xiaojing Li[1, 2], Shouwen Zhang[4, 6], Yi Li[5, 6], Xinrong Chen[4, 6], Youmin Tang[3, 1], Dake Chen[1]

[1] State Key Laboratory of Satellite Ocean Environment Dynamics, Second Institute of Oceanography, Ministry of Natural Resources, Hangzhou 310012, China

[2] Southern Marine Science and Engineering Guangdong Laboratory (Zhuhai), Zhuhai 519080, China

[3] Environmental Science and Engineering, University of Northern British Columbia, Prince George V2N 4Z9, Canada

[4] National Marine Environmental Forecasting Center, Beijing 100081, China

[5] College of Oceanography, Hohai University, Nanjing 210098, China

[6] Key Laboratory of Marine Hazards Forecasting of Ministry of Natural Resources, Hohai University, Nanjing 210098, China

Received 26 February 2021; accepted 11 May 2021

Abstract

A new nudging scheme is proposed for the operational prediction system of the National Marine Environmental Forecasting Center (NMEFC) of China, mainly aimed at improving El Niño–Southern Oscillation (ENSO) and Indian Ocean Dipole (IOD) predictions. Compared with the origin nudging scheme of NMEFC, the new scheme adds a nudge assimilation for wind components, and increases the nudging weight at the subsurface. Increasing the nudging weight at the subsurface directly improved the simulation performance of the ocean component, while assimilating low-level wind components not only affected the atmospheric component but also benefited the oceanic simulation. Hindcast experiments showed that the new scheme remarkably improved both ENSO and IOD prediction skills. The skillful prediction lead time of ENSO was up to 11 months, 1 month longer than a hindcast using the original nudging scheme. Skillful prediction of IOD could be made 4–5 months ahead by the new scheme, with a 0.2 higher correlation at a 3-month lead time. These prediction skills approach the level of some of the best state-of-the-art coupled general circulation models. Improved ENSO and IOD predictions occurred across all seasons, but mainly for target months in the boreal spring for the ENSO and the boreal spring and summer for the IOD.

Key words: climate prediction system, initialization, prediction skill, ENSO, IOD

Citation: Song Xunshu, Li Xiaojing, Zhang Shouwen, Li Yi, Chen Xinrong, Tang Youmin, Chen Dake. 2022. A new nudging scheme for the current operational climate prediction system of the National Marine Environmental Forecasting Center of China. Acta Oceanologica Sinica, 41(2): 51–64, doi: 10.1007/s13131-021/1857-4

1 Introduction

Low-frequency variability in the ocean-atmosphere system significantly affects global weather and climate anomalies. The earth's strongest interannual climate signal is El Niño–Southern Oscillation (ENSO), which is characterized by anomalous warming in the eastern Pacific and an eastward shift of the upper branch of the Walker Circulation (Philander, 1990). Strong ENSO events cause large numbers of natural disasters worldwide (Huang and Wu, 1989; Ropelewski and Halpert, 1987; Wang, 2002; Zhang et al., 2007). In addition to ENSO, Indian Ocean Dipole (IOD) (Saji and Yamagata, 2002; Saji et al., 1999), which is the strongest interannual variability of the boreal autumn in the Indian Ocean, also has a remarkable impact on the coasts of India, Africa, and Australia (Jourdain et al., 2013; Lim et al., 2017), the Changjiang River Basin and southern China (Xiao et al., 2015; Xie et al., 2009).

With the increasing dependence of economic development on climate, seasonal climate prediction has attracted intense attention from the public, governments, and academics. In recent years, the performance of climate prediction systems have been significantly improved by improvements in model developments, advances in data assimilation techniques, and the availability of observational data. Climate prediction systems are now reliable tools for simulating and predicting the global climate. Many countries have established their own climate prediction systems, including the National Centers for Environmental Prediction

Foundation item: The National Natural Science Foundation of China under contract No. 41690124; the Scientific Research Fund of the Second Institute of Oceanography, Ministry of Natural Resources under contract No. JG2007; the National Natural Science Foundation of China under contract Nos 42006034, 41690120 and 41530961; the Innovation Group Project of Southern Marine Science and Engineering Guangdong Laboratory (Zhuhai) under contract No. 311021009.
*Corresponding author, E-mail: songxs@sio.org.cn

(NCEP) Climate Forecast System (Saha et al., 2014, 2006), the European Centre for Medium-Range Weather Forecasts (ECMWF) (Leutbecher and Palmer, 2008), and the Canadian Global Ensemble Prediction System (Lin et al., 2016). In China, there are two nationally operational systems for ENSO real-time prediction (Tang et al., 2018). One is developed by the National Climate Center, also called the Beijing Climate Center (Wu et al., 2014), and the other is developed by the National Marine Environmental Forecasting Center (NMEFC) (Li et al., 2015). The former issues atmospheric state-related seasonal climate predictions, whereas the latter focuses on oceanic state-related seasonal climate predictions, including ENSO and IOD.

The NMEFC's global climate prediction system, based on the Community Climate System Model 3, was initially developed to offer monthly operational seasonal forecasts in 2008 (Ling et al., 2009). In 2015, Li et al. (2015) upgraded the system to the Community Earth System Model (CESM) and assessed its ENSO forecasting skill. Hindcast results suggested that this prediction system could predict ENSO events well, and the correlation coefficient between the predicted and observed Niño3 index reached 0.7 at 6-month lead (Li et al., 2015). However, there are some concerns with current predictions. For example, the predicted atmospheric response lagged the observations, which might be caused by a lack of atmospheric assimilation in the initial process (Li et al., 2015). Predicted sea surface temperature anomalies (SSTA) in the Indian Ocean has errors over a large area and showed considerable false alarms in time series of IOD mode (Zhang et al., 2018).

The initialization plays a crucial role in seasonal climate prediction. The NMEFC's global climate prediction system currently uses the nudging method for its initialization of operational predicitons, which is also widely used in other operational prediction systems (Chen et al., 1995, 2004; Luo et al., 2005; Zheng et al., 2006; Merryfield et al., 2013; Ren et al., 2017). Considering the importance of assimilating the subsurface temperature in global climate prediction (Tang et al.,2004; Doi et al., 2017; Chen et al., 2020), the NMEFC prediction system assimilates the Global Ocean Data Assimilation System (GODAS) (Saha et al., 2014) subsurface temperature (15–400 m) data. The nudging coefficients of the NMEFC prediction system are designed as the linear function of model layers, from $(10\ \mathrm{d})^{-1}$ at 15 m to $(150\ \mathrm{d})^{-1}$ at ~400 m (Ling et al., 2009; Li et al., 2015). However, because the model layers are dense near the surface and sparse in the subsurface, the nudging efficient decreases quickly with the depth in the mixed layer, and is only about $(75\ \mathrm{d})^{-1}$ at 150 m. This may cause the model to underestimate the subsurface signal in the subsurface and cannot catch possible precursors of climate events without delay. There are two strategies to overcome this shortcoming and increase the observed signal in the subsurface. The first is to enlarge the subsurface nudging coefficients directly, while the second is by forcing the ocean by the atmosphere wind components to modulate the ocean subsurface through the oceanic adjustment (Chen et al., 1995).

This paper combines these two strategies and proposes a new nudging scheme to improve the forecasting performance of the NMEFC's operational climate prediction system. First, wind components below 500 hPa are assimilated into the atmospheric component using the nudging method, and second, the oceanic nudging coefficient profile as a function of depth is modified to increase the weight of subsurface observations.

This paper is organized as follows. Section 2 describes the details of the model and the nudging schemes used in this paper. In sections 3 and 4, the improvements in the initial conditions and the prediction skills are discussed, respectively. Section 5 concludes the paper with a discussion.

2 Model and data

This study used the CESM, version 1.2.1, developed by the National Center for Atmospheric Research and used as the operational climate prediction system by the NMEFC. The CESM couples the atmosphere, ocean, sea ice, rivers, land, and land-ice and supports various resolutions and component configurations. For the atmospheric component, this study used Community Atmosphere Model 4 with a horizontal resolution (f09) of ~0.9°× 1.25° and a 26-layer hybrid sigma-pressure vertical coordinate. For the ocean component, the Parallel Ocean Program 2 model with a horizontal resolution (gx1v6) of ~1.1°×(0.54°–1°) was used. The ocean component had 60 vertical layers, with 10 m intervals in the upper 160 m. Other components used in this study included the Community Land Model, the Los Alamos National Laboratory Sea Ice Model, the Community Ice Sheet Model, and the River Transport Model.

The assimilation method used in the current NMEFC operational prediction system is the nudging method. In this nudging scheme, only subsurface temperature from 15–400 m is assimilated into the ocean. As shown in Fig. 1, the nudging coefficient linearly decreases with the model layers, from $(10\ \mathrm{d})^{-1}$ at 15 m to $(150\ \mathrm{d})^{-1}$ at ~400 m (see the blue line in Fig.1). However, because the model layers are dense near the surface but became sparse with depth, the nudging coefficient rapidly decreases in the mixed layer and is only $(75\ \mathrm{d})^{-1}$ at 150 m (see Fig. 1). This may cause a lack of subsurface signal in the initialization, which results in the rapid decrease of prediction skill with a long lead time. In addition, a lack of wind signal in an initialization can lead to a lagged atmospheric response compared to observations (Li et al., 2015).

To overcome these drawbacks, a new nudging scheme was proposed. In the ocean component, the nudging coefficient is profiled with depth as follows:

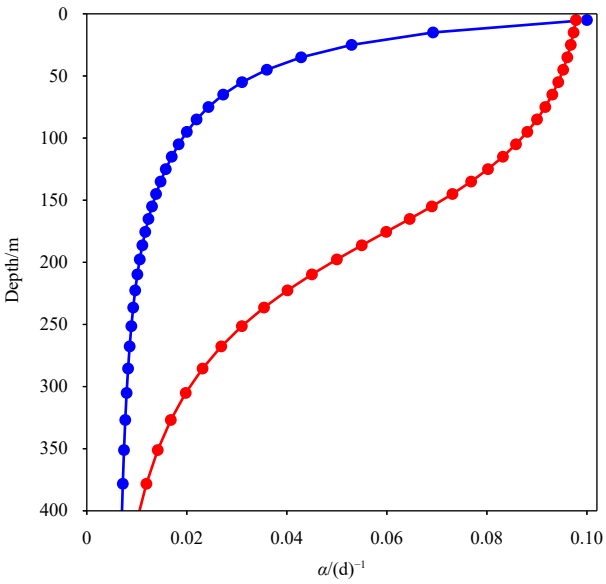

Fig. 1. Nudging coefficient (α) profile for ocean temperature as a function of depth. The dots denote the model layers. Blue and red lines indicate the original and modified scheme.

$$\alpha = 0.05 \times \left[1 + \tanh\left(\frac{20-k}{10}\right)\right], \quad (1)$$

where k is the model layer, and $\tanh(x) = \dfrac{e^x - e^{-x}}{e^x + e^{-x}}$ is the hyperbolic tangent function. This modification significantly increased the nudging coefficient in the upper 150 m (16 layers), and the nudging coefficient only decreased to $(20\ \mathrm{d})^{-1}$ at 150 m (see the red line in Fig. 1). In the new scheme, the temperature from the surface to 400 m (the 31st layer) was nudged into the ocean. For the atmosphere, wind components below 500 hPa were also assimilated using a simple nudging method. The nudging coefficient of wind was chosen as $(6\ \mathrm{h})^{-1}$ below 500 hPa and 0 above 500 hPa.

The effects of the proposed scheme were assessed by three experiments using different assimilation strategies (see Table 1). The CTL-1 and CTL-2 cases only assimilated the upper-layer ocean temperature, using the original and modified nudging coefficient profiles, respectively. The NEW case assimilated both ocean temperature and low-level wind components using the modified nudging coefficient profile. All the experiments assimilated observations between 1980 and 2016, and hindcasts were conducted for every calendar month from January 1982 to December 2016, each lasting 12 months. The forecasted SSTA was calculated by subtracting the climatology of the prediction at the corresponding lead month. Following Zhao and Hendon (2009), a 1-month prediction was defined as the forecast initialized on the first day of the last calendar month.

Monthly mean GODAS temperature data (Saha et al., 2014) and ERA-Interim (Berrisford et al., 2011) 6-hour-resolution wind data were assimilated, and the oceanic and atmospheric datasets were both interpolated into the model grid before the assimilation. Additionally, GODAS sea surface height (SSH) data and ERA-Interim total precipitation data were used for verification purposes.

Table 1. Hindcast experiments

Hindcast case	Assimilation variables	
	Ocean temperature	Wind components
CTL-1	old	×
CTL-2	new	×
NEW	new	√

The temperature anomaly averaged over the eastern Pacific (5°S–5°N, 150°–90°W), the Niño3 index, was used to represent ENSO. The Niño3.4 index was also examined, and it showed similar results. Thus, the Niño3 index was used in this paper unless otherwise indicated. The Dipole Mode Index (DMI), defined as the difference in the SSTA between the western Indian Ocean (WIO, 10°S–10°N, 50°–70°E) and the eastern Indian Ocean (EIO, 0°–10°S, 90°–110°E), was used to measure the variability of IOD (Saji et al., 1999).

3 Initial conditions

The states of the analyses after nudging the observations are examined in this section. Figure 2 shows the time evolution of the observed and simulated zonal wind anomaly at 850 hPa (U850a) in the western Pacific (WP; 5°S–5°N, 140°–180°E) and the Central Indian Ocean (CIO; 5°S–5°N, 70°–90°E) for all three cases. The WP is the key area for westerly wind bursts (WWB), an important precursor factor for strong El Niño events (Chen et al., 2015), while the zonal wind anomaly in the CIO has a strong relationship with IOD events (Saji and Yamagata, 2002; Saji et al., 1999). Without the assimilation of wind components, the correlation between the observed and the analyses U850a in the CTL-1(CTL-2) case is only 0.67(0.63) in WP and 0.5(0.53) in CIO, respectively. The amplitude of U850a in the CTL-1 and CTL-2 cases was much stronger than the observations for both the WP and the CIO. Specifically, for some strong events (i.e., the 1997 El Niño event and the 1994 and 1997 positive IOD events), the U850a analyses lagged the observations. After assimilating the wind components, for the NEW case, the U850a analyses were in agreement with the observations, suggesting that nudging the low-level wind components was successful.

It is important to include precipitation, a concentrated manifestation of both thermodynamic and dynamic processes in the atmosphere when testing the simulation ability of a model. Figure 3 shows the spatial patterns of the correlation coefficients and root-mean-square errors (RMSEs) for the analyzed precipitation anomaly and the observations for the three cases. The spatial patterns of the correlations and RMSEs for the CTL-1 and

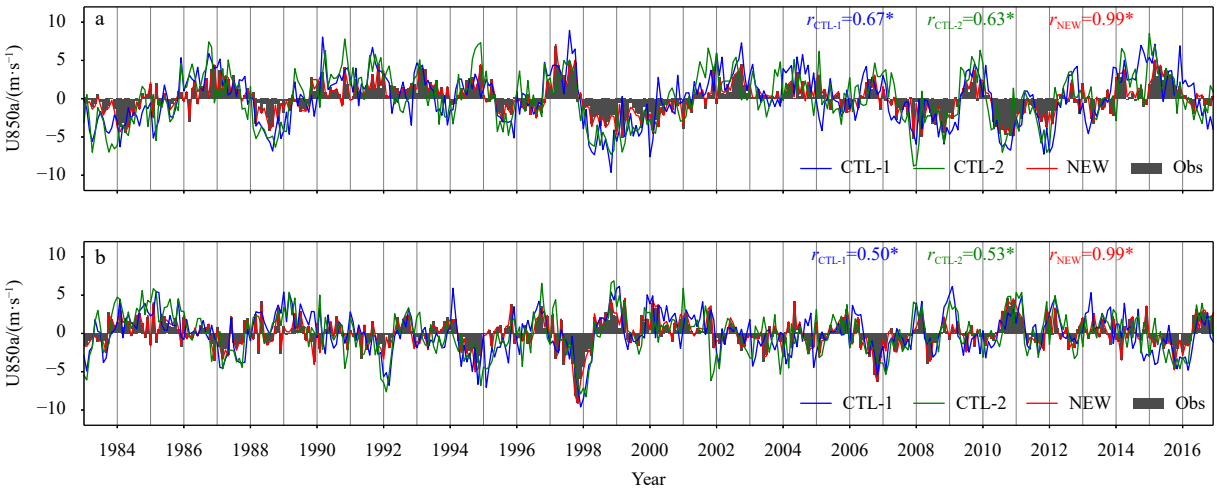

Fig. 2. Time evolution of the U850a in the western Pacific (WP) (a) and the Central Indian Ocean (CIO) (b). The r-values denote the correlation coefficients between the three cases and the observations. The asterisks indicate the correlation coefficient reached a significance level of 0.01 which is calculated based on the effective degrees of freedom (Trenberth, 1984; Zheng et al., 2016).

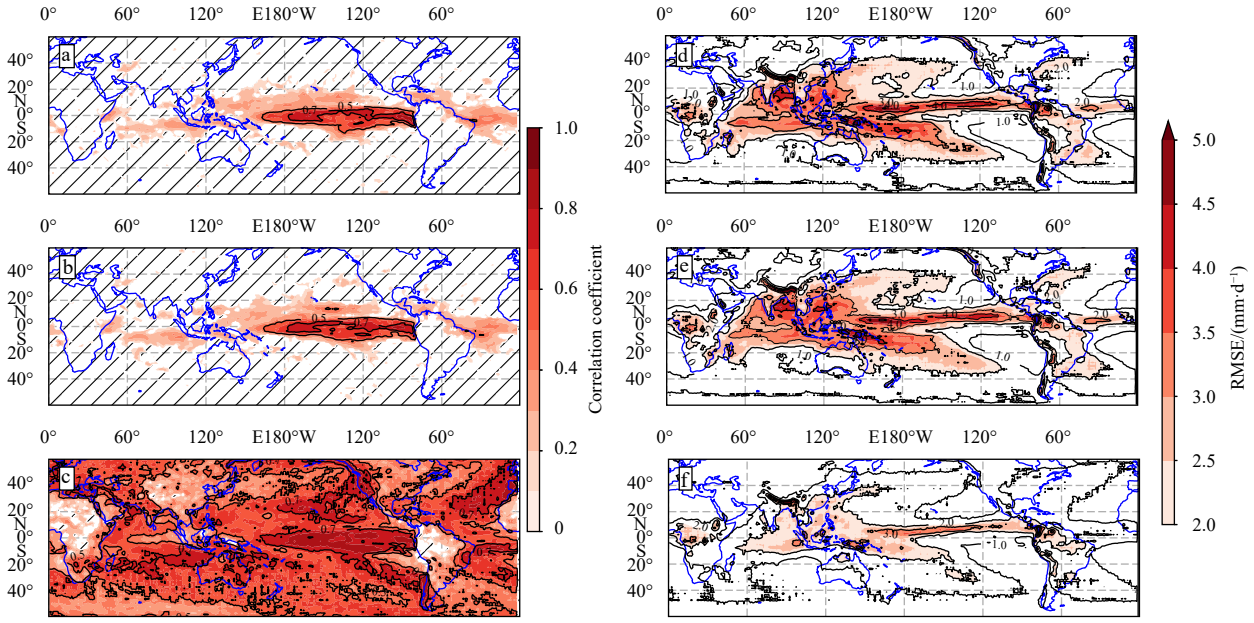

Fig. 3. Spatial correlation coefficient patterns of the analyzed precipitation anomaly and the observations for the CTL-1 (a), CTL-2 (b), and NEW (c) cases. d–f. Same as for a–c but for the root-mean-square errors (RMSEs) of the precipitation anomaly. The areas with slashes indicate that the correlation coefficient does not reach the significance level of 0.01.

CTL-2 cases were similar because both cases did not assimilate the atmospheric data. In these cases, a high correlation of >0.5 was mainly concentrated in a narrow belt around the equatorial Pacific Ocean, while a large RMSE appeared in the intertropical convergence zone and the tropical warm pool where the convections are active. The improvement of the NEW scheme was impressive, with a correlation larger than 0.5 over almost the entire domain. The RMSE of the NEW case was also reduced from over 3 mm/d to 2 mm/d in the tropical warm pool. Considering that precipitation was not directly assimilated into the model, such improvements in the assimilation analyses clearly showed the superiority of assimilating low-level wind components in the atmospheric model.

Figure 4 shows the correlation coefficients and RMSEs for the along-equator analyses of the ocean temperature anomaly for the three cases and the corresponding observations. For the CTL-1 case, high correlation levels were mainly distributed in the upper 100 m in the Pacific, but the correlation decreased rapidly with increasing depth, and a large RMSE, which mainly appeared in the subsurface, was distributed along the thermocline, with values over 1°C. This confirmed the previous assumption that the rapid decrease of the nudging coefficient in the subsurface would lead to poor performance when representing the subsurface temperature. For the CTL-2 case, the subsurface correlation was sig-

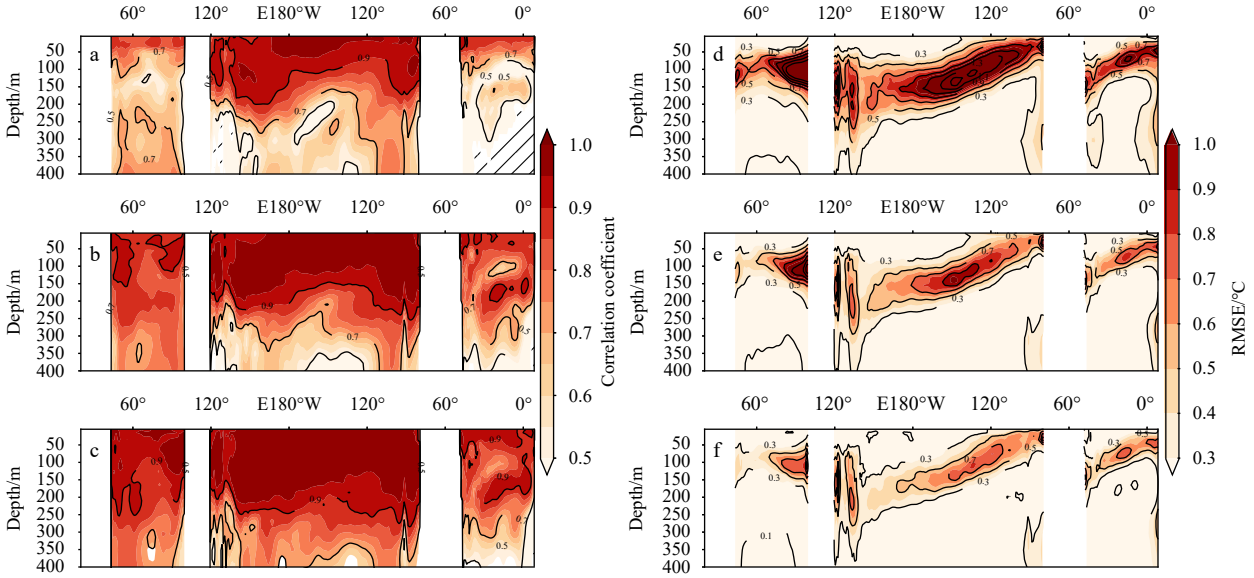

Fig. 4. Correlation coefficients for the ocean temperature analysis and the observations along the equator for the CTL-1 (a), CTL-2 (b), and NEW (c) cases. d–f. Root-mean-square errors (RMSEs) for a–c. The areas with slashes indicate that the correlation coefficient does not reached the significance level of 0.01.

nificantly increased compared with the CTL-1 case, while the large RMSEs in the thermocline were remarkably reduced from over 1.2°C to about 0.8°C. This was not surprising because the nudging coefficient in the subsurface was enlarged in the CTL-2 case. A comparison of the CTL-2 and NEW cases showed that the simulation of the upper ocean temperature was further improved after nudging the low-level wind components. Specifically, the RMSEs of the eastern Indian Ocean thermocline were reduced by about 40%, from over 1°C to about 0.6°C. This improvement was due to adjusting the ocean with the realistic wind components instead of directly nudging the oceanic observations.

The SSH anomaly was affected by both oceanic- and thermodynamic variables, including currents, pressure, temperature, and salinity; therefore, it was a good measurement for assessing the performance of the assimilation. Figure 5 shows the spatial pattern of the correlation coefficients and RMSEs over 60°S–60°N between an SSH anomaly analysis and the observational counterparts at initial times for these three experiments. For the CTL-1 case, high correlation coefficients (>0.8) were distributed in the tropical Pacific and the southern Indian Ocean, suggesting a reasonable adjustment of the SSH anomaly by the assimilation of the ocean temperature there. However, adjusting the temperature assimilation to the SSH anomaly was not sufficient in other regions, particularly in the northwestern Indian Ocean and the northern Atlantic Ocean, resulting in correlations as low as 0.4. The RMSEs of the SSH anomaly were more than 5 cm in the north equatorial Pacific, the south equatorial Indian Ocean, and the western boundary current areas, suggesting poor ocean adjustment in these areas. Compared with the CTL-1 case, the correlation of the SSH anomaly in the CTL-2 case was improved, with a value of more than 0.8 over almost the entire tropical Pacific, and the RMSEs in the tropical Pacific and the Indian Ocean were reduced to 3–4 cm. For the NEW case, the performance of the simulated SSH anomaly was further improved compared with the CTL-2 case. The correlation coefficient of the SSH anomaly was as high as 0.9 in the most tropical Pacific and the southern and the eastern Indian Ocean, while the RMSEs in most domains were less than 3 cm, except for the western boundary current areas. In the northwestern Indian Ocean, the correlation was remarkably improved, from 0.6 in the CTL-2 case to over 0.8 in the NEW case. This was because monsoons play an important role in modulating the interannual variation of the Indian Ocean (Jourdain et al., 2013). The difference between the CTL-2 case and the NEW case indicated that the assimilated low-level wind components had improved the initial conditions of the ocean.

In summary, the NEW case included two modifications: increasing the nudging weight of the subsurface temperature and assimilating low-level wind components. The effect of increasing the weight of the subsurface temperature assimilation was mainly observed in the ocean: it improved the model's performance by directly simulating the subsurface temperature and modulating the ocean dynamic states through the ocean adjustment. Assimilation of the low-level wind components not only significantly improved the simulation performance of the atmospheric model but also modulated the dynamics of the upper ocean by forcing the ocean.

4 Prediction skill

In this section, prediction skill for two high-impact interannual variabilities, ENSO and IOD, is examined, and the improvement of the NEW nudging scheme is analyzed.

4.1 *ENSO prediction skill*

To assess the ENSO prediction skill, the Niño3 index is used to present ENSO, and the correlation and RMSE skills between the observed and forecasted Niño3 index are shown as a function of lead time in Fig. 6. The persistence of the prediction skill is also presented for reference. The correlation and RMSE skills of all three cases were better than the persistence skill. If the threshold value of the skillful prediction is defined as the correlation of 0.5, which is equivalent the level of statistical significance at the 99% confidence level with an intenpdendent sample size of 30, the skillful prediction for ENSO can reach up to the 10-month lead time, suggesting reliable forecasting of the ENSO by these

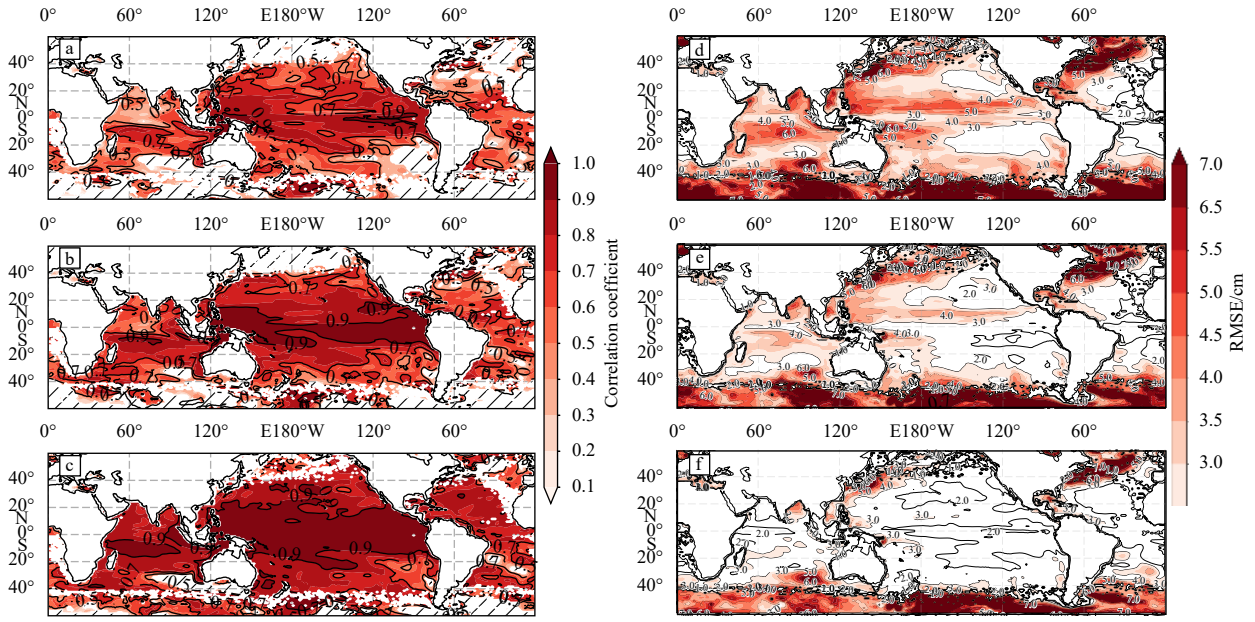

Fig. 5. Spatial correlation coefficient patterns for the analyzed sea surface height (SSH) anomaly and the Global Ocean Data Assimilation System (GODAS) counterpart for the CTL-1 (a), CTL-2 (b), and NEW (c) cases. d–f. Root-mean-square errors (RMSEs) of the SSH anomaly for a–c. The areas with slashes indicate that the correlation coefficient does not reach the significance level of 0.01.

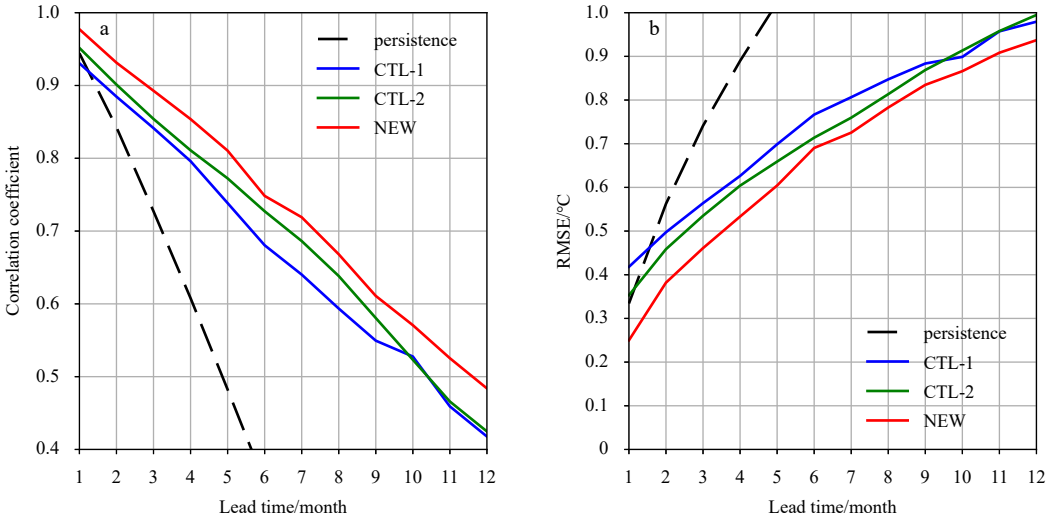

Fig. 6. Correlation coefficients (a) and root-mean-square errors (RMSEs) (b) of the observed and forecasted Niño3 indices as a function of lead time for all three cases.

three cases. After enlarging the subsurface temperature nudging coefficient, the prediction skill of the CTL-2 case was better than that of the CTL-1 case for a lead time smaller than 9 months. This indicated that the CTL-1 case may underestimate the subsurface signal in the ocean and increasing the assimilation weight of subsurface temperature can effectively overcome this. The NEW case had the best prediction skill compared to the two other cases, and a comparison with the CTL-2 case suggested the beneficial impact of assimilating wind components on the ENSO prediction, and the lead time of skillful prediction increased to over 11 months. To emphasize the major improvements in the NEW case, the differences between the original CTL-1 case and the NEW case is discussed in the following sections.

ENSO predictability is usually seasonally dependent, with significant low prediction skill during spring, called the spring prediction barrier (Chen et al., 2000; Luo et al., 2005; Zhang et al., 2005). Figure 7 shows the correlation skill of the observed and forecasted Niño3 index as a function of the initial month and the lead time. Compared to the CTL-1 case, the NEW case was improved for most lead and initial times, particularly for ENSO prediction target on the boreal spring and summer (Fig. 7c); the boreal spring prediction barrier was greatly alleviated. For example, in the CTL-1 scheme, the correlation skill of a November initialized prediction rapidly dropped from 0.8 in February to 0.5 in May. In contrast, in the NEW scheme, the correlation skill only dropped slightly across spring and was maintained above 0.5 for all lead times. For the predictions initialized at boreal spring and summer, the ENSO prediction skills were also improved for the short lead times, suggesting that the effects of improving the initial conditions.

Figure 8 shows the observed Niño3 index along with the 3-, 6-, and 9-month lead predictions. Both the CTL-1 and NEW schemes predicted major ENSO events with at least a 9-month lead, including El Niño events in 1982/1983, 1986/1987, 1991/1992, 1997/1998, and 2015/2016 and La Niña events in 1988/1989, 1995/1996, 1999/2000, 2007/2008, and 2010/2011. A comparison of the CTL-1 case with the NEW case showed that the NEW case had fewer false alarms and could better predict the amplitude of some events, particularly those with long lead times (i.e., El Niño events in 1997/1998 and 2009/2010 with a 9-month lead). For the three strongest El Niño events in the last 35 years (i.e., 1982/1983, 1997/1998, and 2015/2016), the NEW scheme had a stronger and more realistic amplitude prediction than the CTL scheme for lead times longer than 6 months.

To explore possible mechanisms behind the improvement of the NEW scheme, the 1997 prediction ,which was the second strongest El Niño event, and its amplitude prediction had the largest improvement at the 6- and 9-month lead, was examined. Figure 9a shows the time–longitude diagram of the observed SSTA, the SSH anomaly, and the wind components along the equator during the 1997 El Niño event. In the boreal spring of 1997, strong westerly wind (i.e., WWB) appeared to the west of the dateline, resulting in the accumulation of warm water near the dateline that propagated to the east through equatorial Kelvin waves. During the boreal autumn, the El Niño event, developed through Bjerknes feedback, reached its mature phase in the boreal winter. For the CTL-1 case, the strong westerly wind could not be captured in the initial field by only assimilating the ocean temperature because WWB is a semi-random process that cannot be adequately simulated. Due to the lack of WWB in the onset phase, the SSH anomaly simulated in the CTL-1 case was much weaker than the observations, so the amplitude of the El Niño event was underestimated. The NEW scheme, by assimilating wind data, significantly improved the model states in the boreal spring, including an accurate westerly wind and a stronger SSTA and SSH anomaly. Thus, the forecasted El Niño in the NEW scheme was stronger and more realistic than that for the CTL-1 case.

4.2 *IOD prediction skill*

It has been reported that prediction skill for the interannual variability of the Indian Ocean is much lower than that for the Pacific Ocean (Luo et al., 2005; Zhao and Hendon, 2009). Figure 10 shows the prediction skill of the DMI. For the original CTL-1 case, the prediction skill of the DMI was worse than the persistence skill, indicating poor prediction performance. The prediction performance of the CTL-2 case was significantly improved, indicating the importance of the subsurface signals. Similar to the ENSO prediction skill, the NEW case had the best prediction skill of the three cases: the correlation coefficient at the 3-month lead was about 0.65, which was about 0.2 higher than for the CTL-1

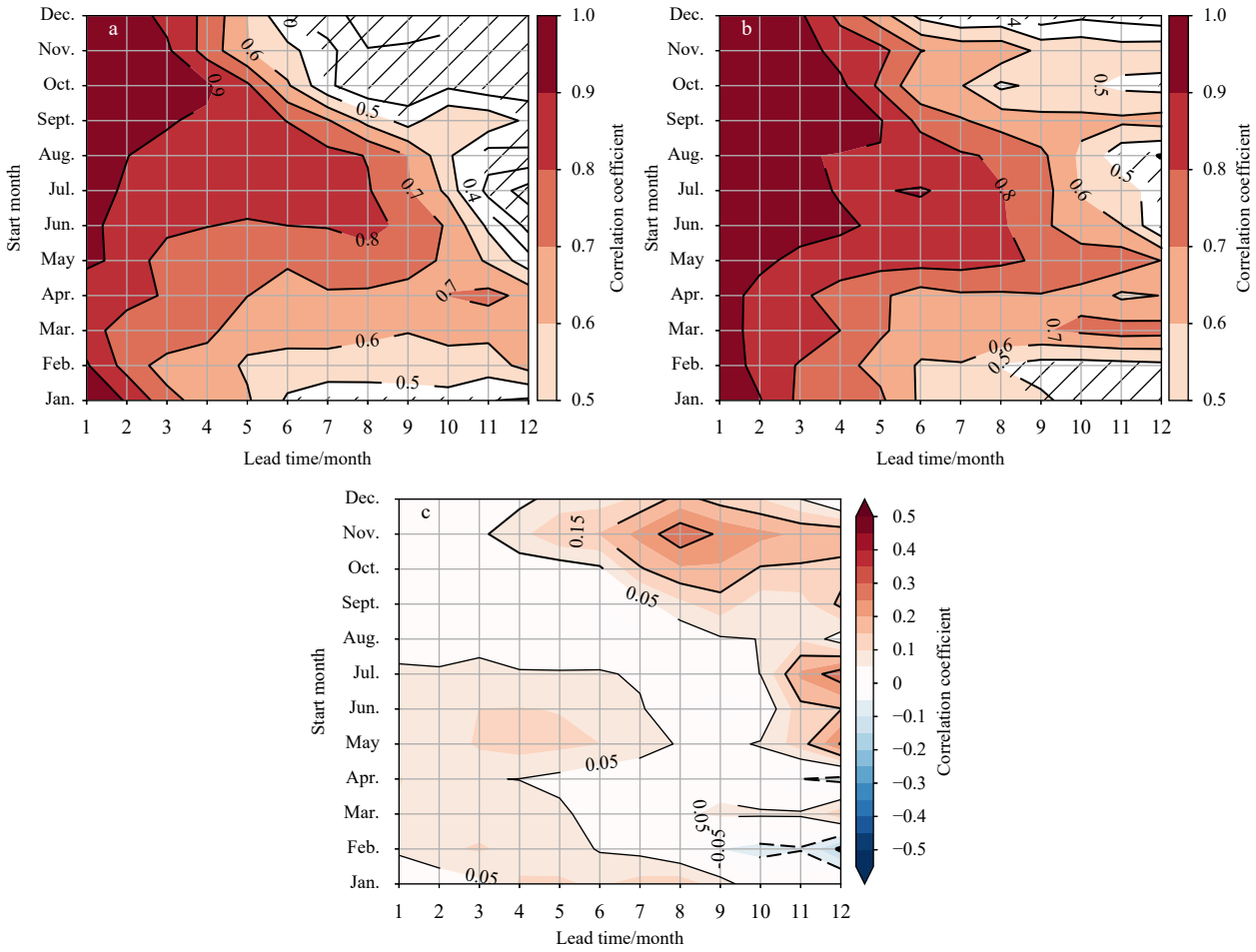

Fig. 7. Correlation skill of the Niño3 index as a function of lead time and start month. The CTL-1 case (a) and the NEW case (b). c. The correlation skill difference between the NEW case and the CTL-1 case. The areas with slashes indicate that the correlation coefficient does not reach the significance level of 0.01.

case. The skillful prediction period was increased from 2 months in the CTL-1 case to 4–5 months in the NEW case. This level of skill in the NEW scheme was even better than some of the best state-of-the-art coupled general circulation models (CGCMs), where correlations of >0.5 are only maintained for 3- to 4-month leads (Liu et al., 2017; Shi et al., 2012; Wajsowicz, 2005, 2007; Wu and Tang, 2019). The RMSE skill for the NEW scheme was also ~0.1°C smaller than that for the CTL-1 scheme within the 4-month lead, which was ~20% of one standard deviation of the DMI.

The prediction skills for both WIO and EIO are also improved in the NEW case (Figs 10c–f). In the CTL-1 case, the skillful prediction for WIO and EIO can be made about 4 and 3 months ahead, respectively. In the NEW case, the skillful prediction for WIO and EIO exceeds 6 and 5 months, respectively. Comparison of the prediction skill between the two cases reveals that assimilating low-level wind components is more effective in improving the prediction of EIO than that of WIO. One possible reason is that the wind-derived mixing plays an important role in modulating SSTA in the eastern Indian Ocean due to relatively shallow thermocline there (Saji et al., 1999; Vinayachandran et al.,2009), so that assimilating low-level wind components can largely improve the simulation of subsurface states of the initial conditions (Fig. 4).

The correlation skills of the DMI for the CTL-1 and NEW cases as a function of the initial month and lead time are shown in Fig. 11. Consistent with the statistical features shown in Fig. 10, the forecasting skill of the CTL-1 case was lower than that of the NEW scheme for almost all the initial months and lead times. For the CTL-1 case, only forecasts initialized between July and October were skillful for a lead time of 3 months. For the NEW case, skillful predictions exceeding 3 months were achieved for the initial conditions from May to November. The most remarkable improvements occurred for predictions initialized in the boreal spring and summer for short lead times (Fig. 11c), suggesting the importance of the initial process in predicting the onset of IOD events in the boreal spring and summer. However, the winter–spring predictability barrier, characterized by low prediction skill when the prediction was across the boreal winter and spring (Feng and Duan, 2014; Feng et al., 2014; Song et al., 2018), was not significantly improved and persisted in both the CTL-1 and NEW cases, suggesting that this winter–spring prediction barrier of the IOD might be attributed to uncertainties in the physical and dynamical processes rather than initialization conditions.

The observed and predicted DMIs at 2- and 4-month lead times are shown in Fig. 12 for the CTL-1 and NEW cases. Both the CTL-1 and NEW schemes were able to predict strong positive IOD events (e.g., 1994, 1997, 2006, and 2015) at lead times short-

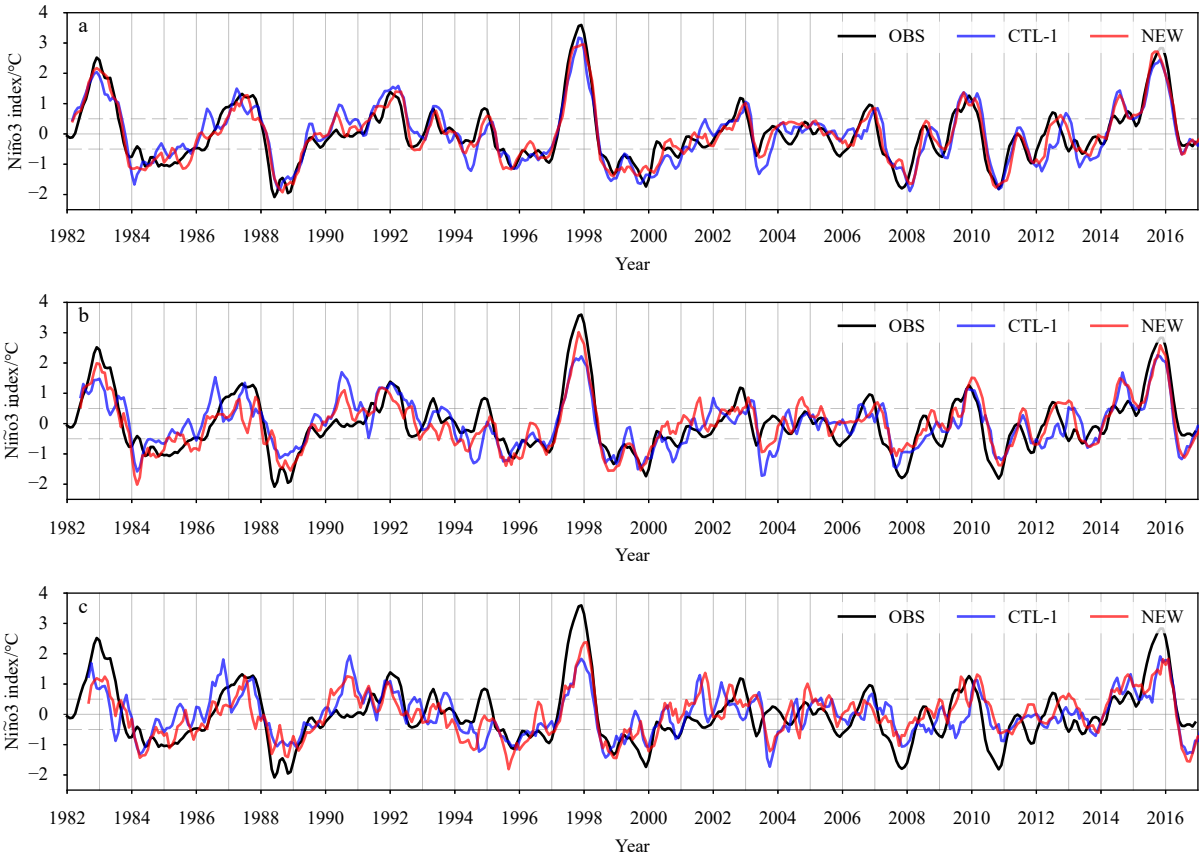

Fig. 8. Time evolution of the observed and predicted Niño3 indices at a 3-month lead time (a). b, c. Same as a but for 6- and 9-month lead times. The dashed lines denote ±0.5°C. All indices have been smoothed using a 3-month running mean.

er than 4 months. However, both cases showed some false alarms in the early 21st century, which has also occurred in other CGCMs (Liu et al., 2017). Compared to the CTL-1 scheme, the NEW scheme produces better amplitude predictions for some

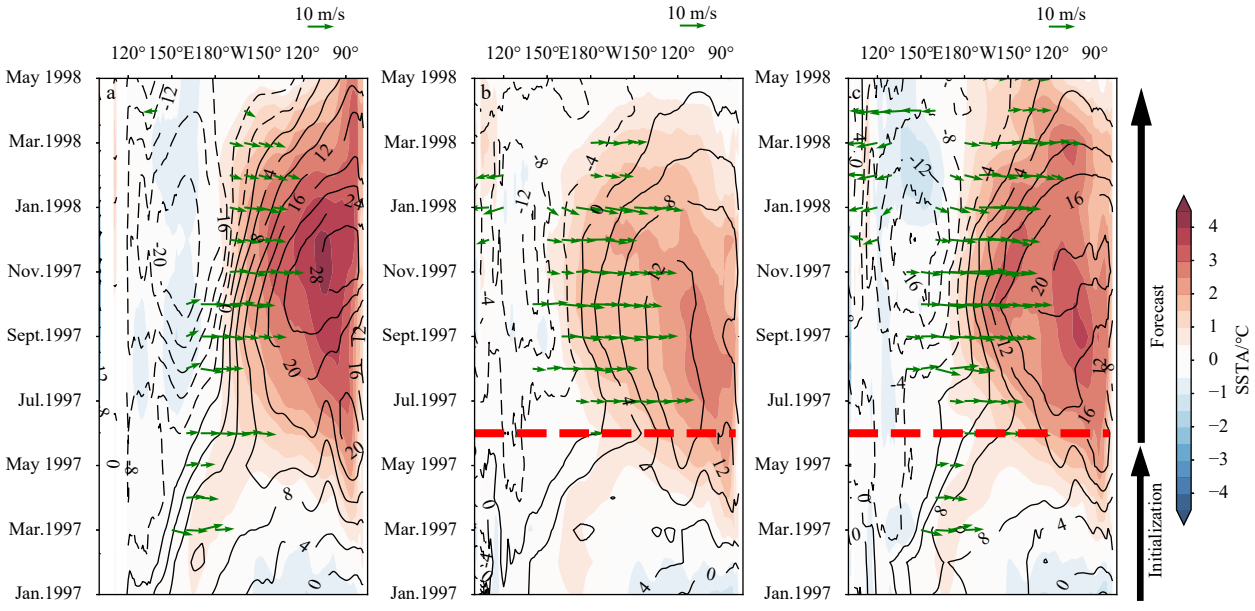

Fig. 9. a. Time evolution of the observed sea surface temperature anomaly (SSTA) (shaded), sea surface height (SSH) anomaly (cm, contoured), and wind components at 850 hPa (vectors) for the equatorial Pacific (2°S–2°N) from January 1997 to May 1998. b. Same as a but for the CTL-1 case prediction initialized in June 1997. Before June 1997, it shows the analyzed states during the initialization process. c. Same as b but for the NEW scheme. The contour interval is 4 cm and only wind speeds larger than 5 m/s are plotted.

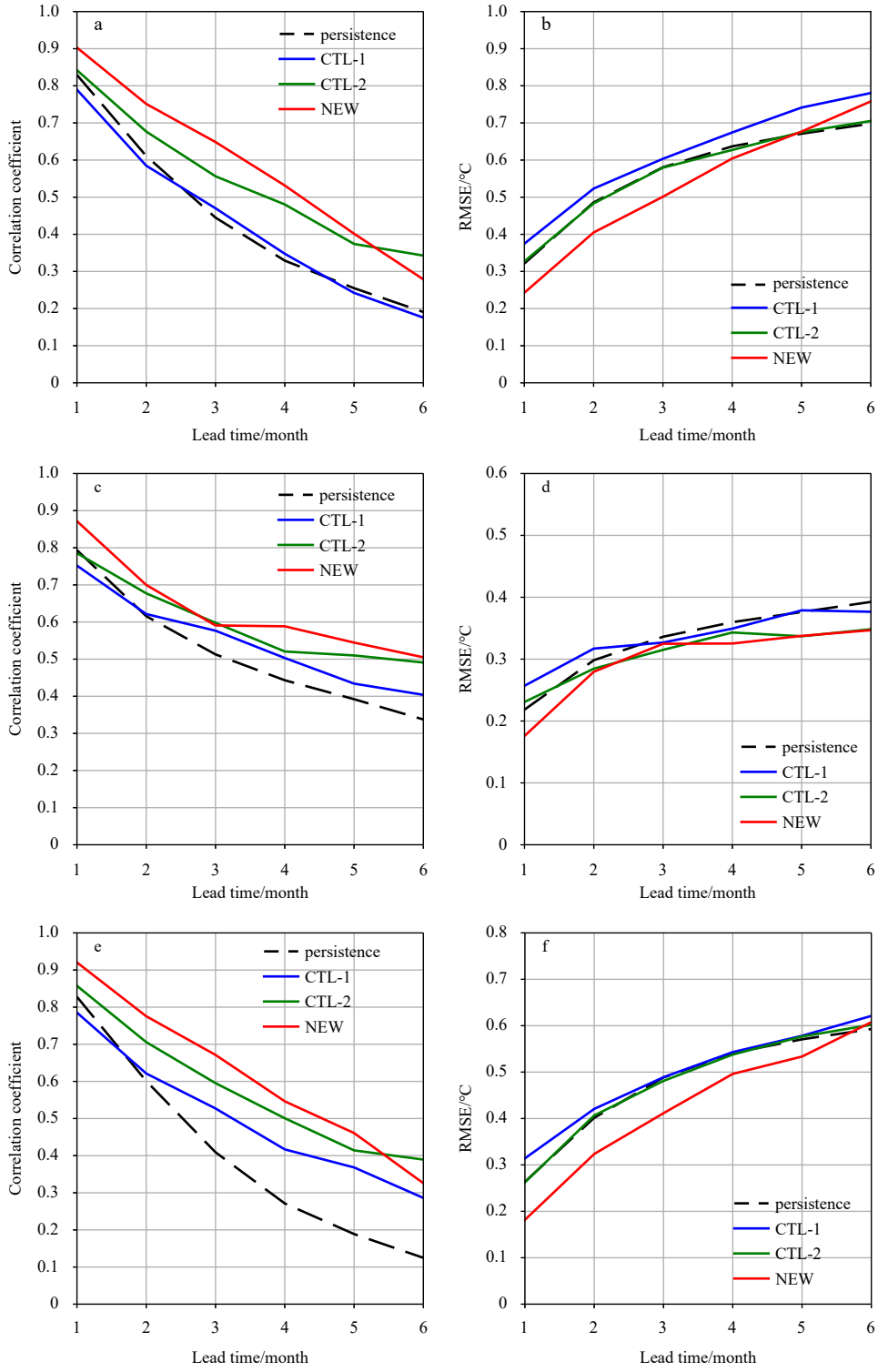

Fig. 10. Correlation coefficients (a) and root-mean-square errors (RMSEs) (b) of the observed and forecasted Dipole Mode Index (DMI) as a function of lead time. c, d. Same as a and b, but for the WIO; e, f. Same as a and b, but for the EIO.

strong IOD events, especially for the lead time of 4 months. For example, the prediction error during the mature phase of the strong positive IOD event of 1994 is reduced from over 1.5°C in the CTL-1 case to about 0.5°C in the NEW case. The same improvement also existed in the prediction for the mature phase of the 1998 negative IOD event. The prediction system predicted the amplitude more accurately in the NEW case than that in the CTL-1 case. As a result, the predicted error was reduced by about 1°C in the NEW case. The NEW scheme also reduced the amplitude errors for false alarms at long lead times compared with the CTL-1 case, including 1986, 1993, and 2014 events. It also successfully predicted some events that the CTL-1 case failed to predict, for example, a 1984 negative IOD event.

Similar to the previous discussion of ENSO prediction, the

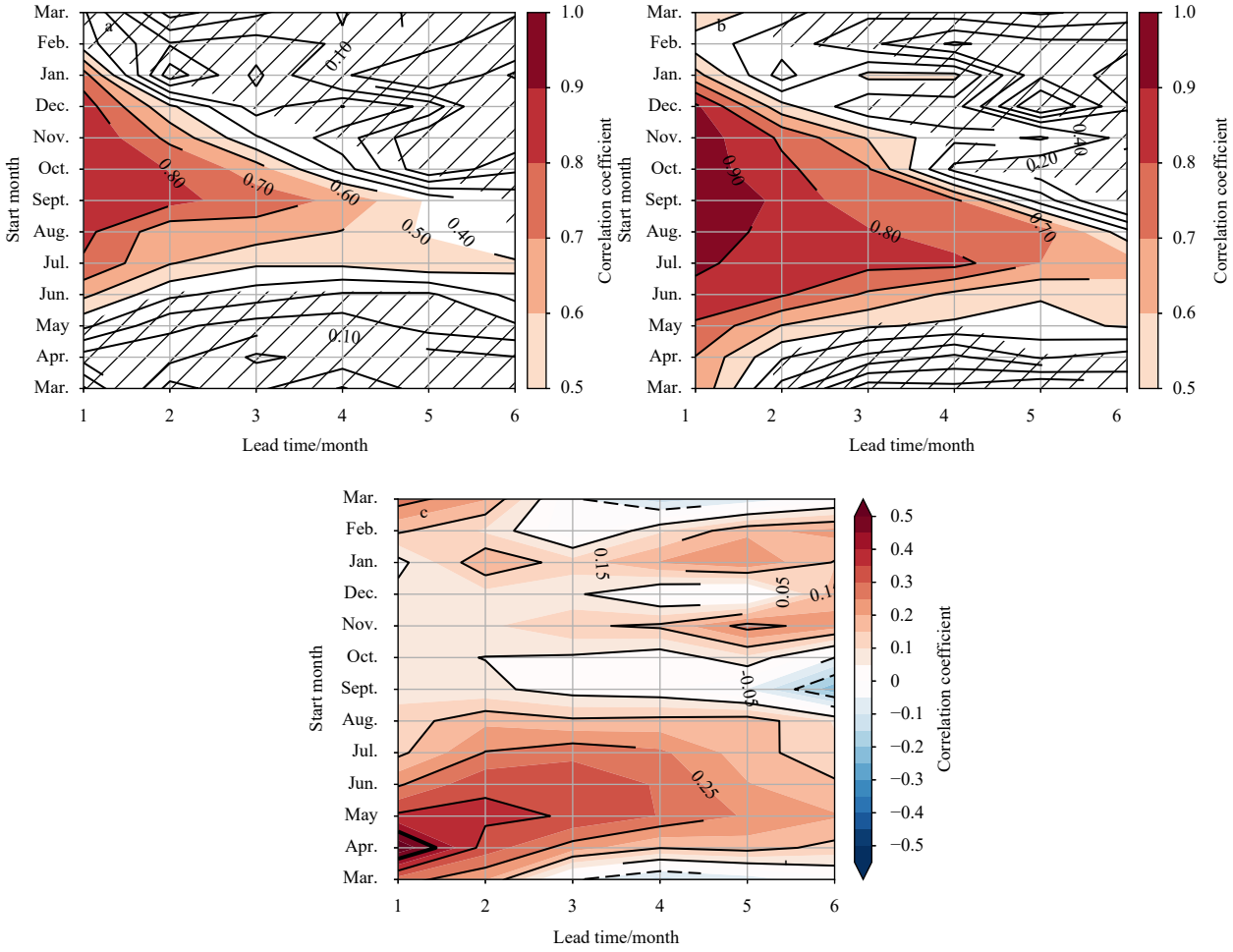

Fig. 11. Correlation skill of the Dipole Mode Index (DMI) as a function of lead time and start month. CTL-1 case (a), NEW case (b), and the correlation skill difference between the NEW case and the CTL-1 case (c). The areas with slashes indicate that the correlation coefficient does not reach the significance level of 0.01.

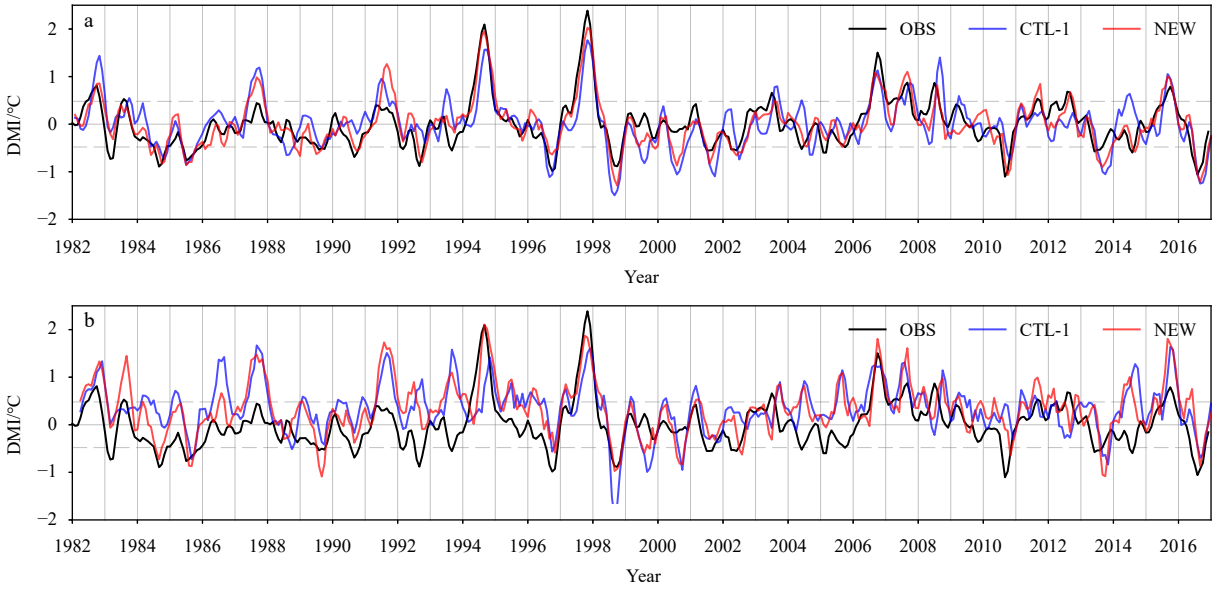

Fig. 12. Time evolution of the observed and predicted Dipole Mode Index (DMI) at the 2-month lead time (a); same as a but for a 4-month lead time (b). The dashed lines denote one standard deviation of the observed DMI (0.48°C). All indices were smoothed using a 3-month running mean.

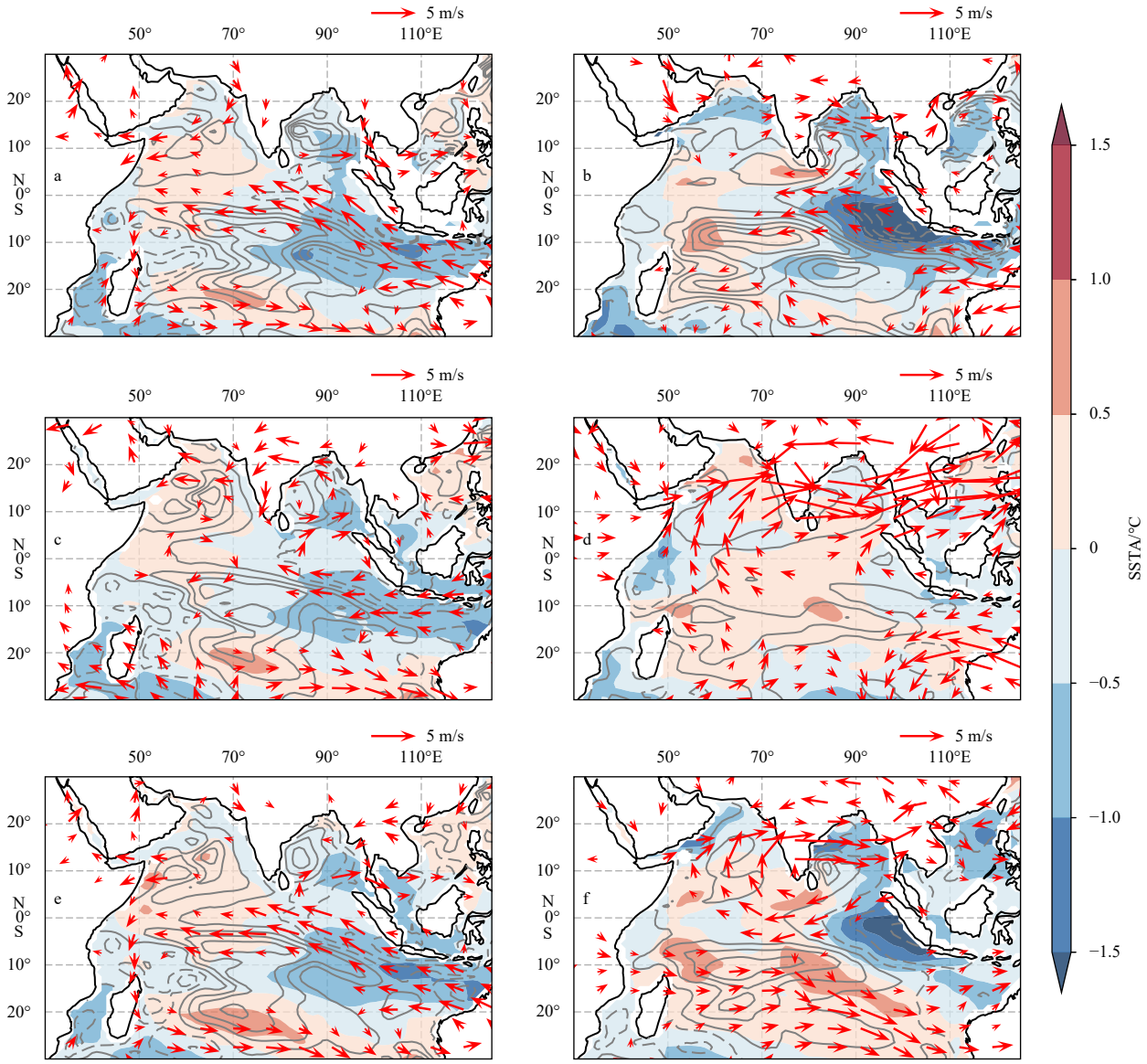

Fig. 13. Observed sea surface temperature anomaly (SSTA) (shaded), sea surface height (SSH) anomaly (contoured), and U850a (vectors) for May 1994 (a) and August 1994 (b); initial conditions for May 1994 in the CTL-1 case (c), and forecasted model states for August 1994 (d). e and f are the same as c and d but for the NEW case. The contour interval is 3 cm and only wind speeds larger than 1 m/s are plotted.

possible mechanisms behind the improvement of IOD prediction by the NEW scheme using an example were also explored. Figure 13 shows the SSTA, the SSH anomaly, and the wind components in the observations and forecasts for the positive 1994 IOD event by the NEW scheme. In May 1994, during the onset phase of a positive IOD event, a strong southeast wind occurred in the equatorial Indian Ocean, corresponding to the dipole of the SSH anomaly and the SSTA between the southeast and the western Indian Ocean. For the CTL-1 case, although the SSTA presented the observed dipole, the variability of the SSH anomaly in the southeastern Indian Ocean and the southeast winds along the equator were underpredicted and showed large negative errors (see black rectangle in Fig. 14a). For the NEW scheme, due to the assimilation of the wind components and the subsurface temperature, the variability of the SSH anomaly in the southeastern Indian Ocean was much stronger than that in the CTL-1 case and closer to the observations (Fig. 14b). This variability of the SSH anomaly leads to long ocean memory and keeps the cooling in the southeastern Indian Ocean, which establishes Bjerknes positive feedback. A strong positive IOD event was successfully predicted to develop and reach maturity by the 4-month lead time, as seen in the observations.

4.3 *Prediction skill of the atmosphere*

The prediction skills of the atmosphere variables in the CTL-1 and NEW cases are also assessed. Figure 15 shows the spatial patterns of the correlation skills for the total precipitable water anomaly (TPWA) at the 1- and 3-month lead. At the 1-month lead, the skillful predictions only occpy a narrow band arround the equatorial Pacific in the CTL-1 case, whereas in the NEW case, the area of skillful predictions extend to the western tropical Pacific, southeastern Indian Ocean and equatorial Atlantic. At the

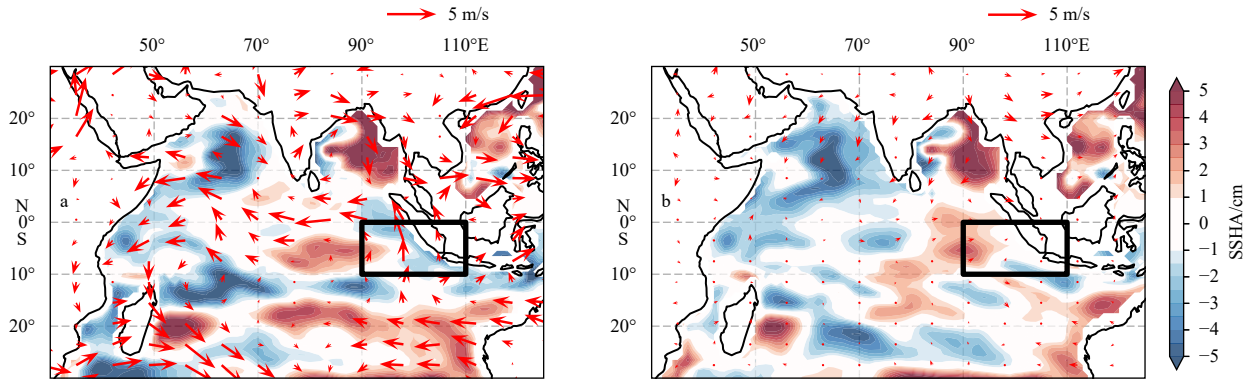

Fig. 14. Initial condition errors of the SSH anomaly (SSHA) (shaded) and U850a (vectors) in the CTL-1 case for the May 1994 (a); b is same as a, but for the NEW case.

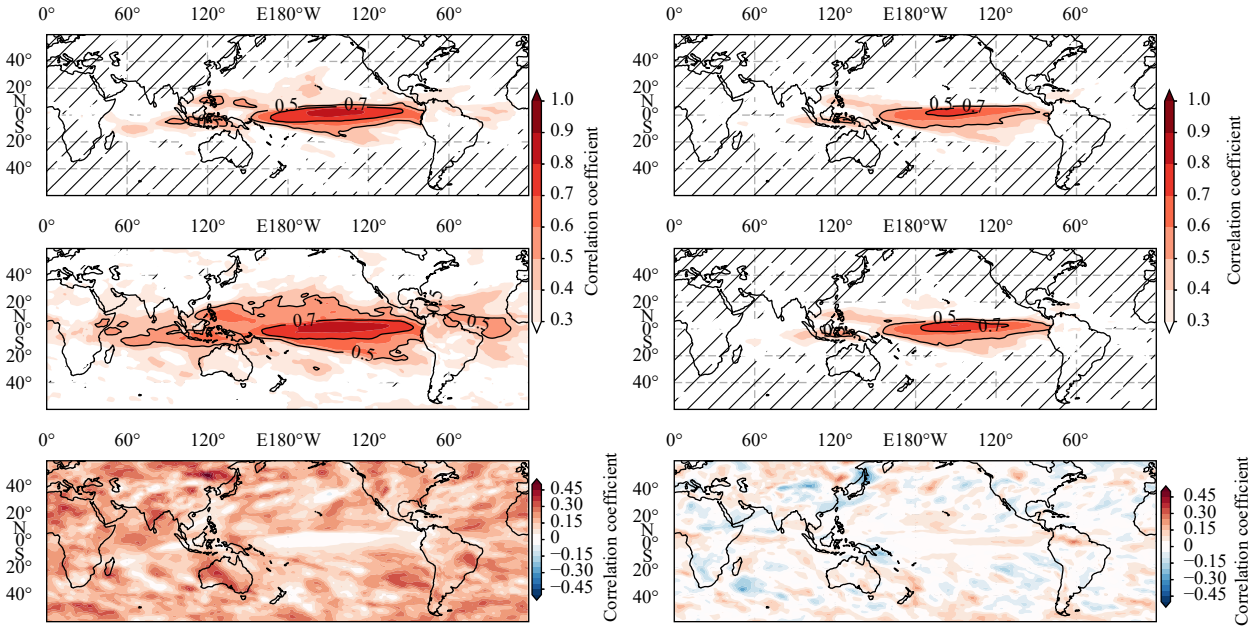

Fig. 15. Spatial pattern of correlation coefficients between the predicted and observed total precipitable water anomalies (TPWA) at the 1-month (left column) and 3-month (right column) lead times, for the CTL-1 (the first row) and NEW cases (the second row), respectively. The third row indicates the difference between the NEW case and CTL-1 case. The areas with slashes indicate that the correlation coefficient does not reach the significance level of 0.01.

3-month lead time, the TPWA has skillful prediction only at the equatorial Pacific in both the CTL-1 and NEW cases. For other atmospheric variables, such as U850a, the prediction performance in these two cases is quite similar (not shown). Thus, the nudging atmospheric winds can mainly improve the short-range climate predictions within 3 months. This may be attributed to the short-term memory of atmospheric signals and the large atmospheric model bias outside the equatorial Pacific.

5 Discussion and conclusions

This paper aimed to improve the prediction skills of the operational NMEFC prediction system using a modified nudging scheme. The proposed scheme brought two improvements to the initialization process. First, the vertical profile of the nudging coefficients for ocean temperature was modified by increasing the weights of the subsurface nudging coefficients. Second, low-level wind components were assimilated into the atmospheric component of CESM using the nudging method. Compared to the original scheme, the new scheme significantly improved the atmospheric and oceanic analyses, particularly for tropical regions. Increasing the subsurface nudging weight mainly affected the ocean component, while assimilating the wind components improved not only the simulation performance of the atmosphere component but also the ocean dynamic states through forcing the ocean. This suggests that the joint nudging of atmospheric and oceanic variables more realistically represents oceanic and atmospheric physical processes and interactions.

Hindcast experiments, conducted for 1982–2016, were initialized using the different schemes. The results showed that the NEW scheme effectively improved ENSO and IOD forecasting. The prediction skills of the Niño3 index in the NEW case gave the highest prediction skills among three cases, with an effective forecast time over 11 months. The new scheme also significantly increased the prediction skill of ENSOs initialized during the boreal autumn and winter with long lead times. Improvement in the IOD prediction skill was more impressive. Compared with the

original scheme of the CTL-1 case, the new scheme increased the prediction skill up to 0.2 for correlations with a 3-month lead and decreased the RMSEs by ~0.1°C, equivalent to 20% of the standard deviation of the DMI. Using the new scheme, skillful predictions of the IOD using the new scheme can be made up to 4–5 months ahead, which is better than that of some current state-of-art CGCMs (Liu et al., 2017; Wu and Tang, 2019). The predicted IOD events using the new scheme also showed more realistic amplitudes and fewer false alarms.

The reason why the new scheme was better than the original scheme may be attributed to its enhanced ability to capture precursor factors and their effects on ocean memories. Recent studies have suggested that precursor factors in the atmosphere and ocean, such as WWBs at the equator, the accumulation of warm water in the WP, and the Madden–Julian oscillation, are important for the development and prediction of ENSO and IOD events (Chen et al., 2015; Hu and Fedorov, 2019; Luo et al.,2008; Kug et al., 2009; Rao et al., 2009; Tan et al., 2020). These precursor factors are difficult to represent and simulate well in current CGCMs, and the effects of these precursor factors on ocean states were also underestimated in the ocean component. Thus, this is an effective way to directly assimilate multiple observations in both the atmospher and ocean componetss to capture these precursor processes.

Initialization is critically important for seasonal climate predictions. Nudging is a simple and widely used method for conducting operational prediction systems (Li et al., 2015; Luo et al., 2005; Merryfield et al., 2013; Ren et al., 2017). However, the shortcomings of the nudging method are also obvious. The choice of the nudging coefficient is subjective, and it is hard to obtain perfect values. This study suggests that joint, weak coupled assimilation of multi-source observations can modulate the dynamic states in the subsurface through model adjustment, which can finally improve assimilation and prediction performance.

To obtain better initial conditions, efforts have been directed toward offering good and accurate initial conditions for coupled models with the application of advanced assimilation methods and multiple-source observations in recent years. Currently, many operational prediction centers use complex assimilation methods, including 3D/4D-var (e.g., the NCEP and the ECMWF) and the ensemble Kalman filter, to produce initial conditions. These centers also operationally apply ensemble predictions using optimal perturbations. Compared to advanced countries, seasonal climate prediction is still at an early stage in China. This work is the first attempt to improve operational seasonal climate prediction in China using both atmospheric and oceanic observational datasets. The development of an operational assimilation system using an ensemble adjustment Kalman filter, which allows for the assimilation of multiple atmospheric and oceanic observations within the framework of coupling assimilation, is the ultimate goal and already under the way. Nevertheless, this work, by offering a significant improvement to the initialization scheme currently used by the NMEFC, has made an important contribution with practical significance.

References

Berrisford P, Dee D P, Poli P, et al. 2011. The ERA-Interim archive, version 2.0. https://www.ecmwf.int/node/8174[2011-11/2020-09]

Chen Dake, Cane M A, Kaplan A, et al. 2004. Predictability of El Niño over the past 148 years. Nature, 428(6984): 733–736, doi: 10.1038/nature02439

Chen Dake, Cane M A, Zebiak S E, et al. 2000. Bias correction of an ocean-atmosphere coupled model. Geophysical Research Letters, 27(16): 2585–2588, doi: 10.1029/1999GL011078

Chen Dake, Lian Tao, Fu Congbin, et al. 2015. Strong influence of westerly wind bursts on El Niño diversity. Nature Geoscience, 8(5): 339–345, doi: 10.1038/ngeo2399

Chen Xingrong, Wang Hui, Zheng Fei, et al. 2020. An ensemble-based SST nudging method proposed for correcting the subsurface temperature field in climate model. Acta Oceanologica Sinica, 39(3): 73–80, doi: 10.1007/s13131-020-1568-2

Chen Dake, Zebiak S E, Busalacchi A J, et al. 1995. An improved procedure for EI Niño forecasting: Implications for predictability. Science, 269(5231): 1699–1702, doi: 10.1126/science.269.5231.1699

Doi T, Storto A, Behera S K, et al. 2017. Improved prediction of the Indian Ocean Dipole mode by use of subsurface ocean observations. Journal of Climate, 30(19): 7953–7970, doi: 10.1175/JCLI-D-16-0915.1

Feng Rong, Duan Wansuo. 2014. The spatial patterns of initial errors related to the "winter predictability barrier" of the Indian Ocean Dipole. Atmospheric and Oceanic Science Letters, 7(5): 406–410, doi: 10.1080/16742834.2014.11447198

Feng Rong, Duan Wansuo, Mu Mu. 2014. The "winter predictability barrier" for IOD events and its error growth dynamics: Results from a fully coupled GCM. Journal of Geophysical Research: Oceans, 119(12): 8688–8708, doi: 10.1002/2014JC010473

Hu Shineng, Fedorov A V. 2019. The extreme El Niño of 2015–2016: the role of westerly and easterly wind bursts, and preconditioning by the failed 2014 event. Climate Dynamics, 52(12): 7339–7357, doi: 10.1007/s00382-017-3531-2

Huang Ronghui, Wu Yifang. 1989. The influence of ENSO on the summer climate change in China and its mechanism. Advances in Atmospheric Sciences, 6(1): 21–32, doi: 10.1007/BF02656915

Jourdain N C, Gupta A S, Taschetto A S, et al. 2013. The Indo-Australian monsoon and its relationship to ENSO and IOD in reanalysis data and the CMIP3/CMIP5 simulations. Climate Dynamics, 41(11): 3073–3102

Kug J S, Sooraj K P, Jin Feifei, et al. 2009. Impact of Indian Ocean Dipole on high-frequency atmospheric variability over the Indian Ocean. Atmospheric Research, 94(1): 134–139, doi: 10.1016/j.atmosres.2008.10.022

Leutbecher M, Palmer T N. 2008. Ensemble forecasting. Journal of Computational Physics, 227(7): 3515–3539, doi: 10.1016/j.jcp.2007.02.014

Li Yi, Chen Xingrong, Tan Jing, et al. 2015. An ENSO hindcast experiment using CESM. Haiyang Xuebao (in Chinese), 37(9): 39–50

Lim E P, Hendon H H, Zhao Mei, et al. 2017. Inter-decadal variations in the linkages between ENSO, the IOD and south-eastern Australian springtime rainfall in the past 30 years. Climate Dynamics, 49(1): 97–112

Lin Hai, Gagnon N, Beauregard S, et al. 2016. GEPS-based monthly prediction at the Canadian meteorological centre. Monthly Weather Review, 144(12): 4867–4883, doi: 10.1175/MWR-D-16-0138.1

Ling Tiejun, Wang Zhanggui, Wang Bin, et al. 2009. Assimilation modeling by using CCSM3 model. Haiyang Xuebao (in Chinese), 31(6): 9–21

Liu Huafeng, Tang Youmin, Chen Dake, et al. 2017. Predictability of the Indian Ocean Dipole in the coupled models. Climate Dynamics, 48(5): 2005–2024

Luo Jingjia, Behera S, Masumoto Y, et al. 2008. Successful prediction of the consecutive IOD in 2006 and 2007. Geophysical Research Letters, 35(14): L14S02

Luo Jingjia, Masson S, Behera S, et al. 2005. Seasonal climate predictability in a coupled OAGCM using a different approach for ensemble forecasts. Journal of Climate, 18(21): 4474–4497, doi: 10.1175/JCLI3526.1

Merryfield W J, Lee W S, Boer G J, et al. 2013. The Canadian seasonal to interannual prediction system. Part I. Models and initialization. Monthly Weather Review, 141(8): 2910–2945, doi: 10.1175/

MWR-D-12-00216.1
Philander S G. 1990. El Nino, La Nina, and the Southern Oscillation. San Diego, CA, USA: Academic Press
Rao S A, Luo Jingjia, Behera S K, et al. 2009. Generation and termination of Indian Ocean Dipole events in 2003, 2006 and 2007. Climate Dynamics, 33(6): 751–767, doi: 10.1007/s00382-008-0498-z
Ren Hongli, Jin Feifei, Song Lianchun, et al. 2017. Prediction of primary climate variability modes at the Beijing Climate Center. Journal of Meteorological Research, 31(1): 204–223, doi: 10.1007/s13351-017-6097-3
Ropelewski C F, Halpert M S. 1987. Global and regional scale precipitation patterns associated with the El Niño/southern oscillation. Monthly Weather Review, 115(8): 1606–1626, doi: 10.1175/1520-0493(1987)115<1606:GARSPP>2.0.CO;2
Saha S, Moorthi S, Wu Xingren, et al. 2014. The NCEP climate forecast system version 2. Journal of Climate, 27(6): 2185–2208, doi: 10.1175/JCLI-D-12-00823.1
Saha S, Nadiga S, Thiaw C, et al. 2006. The NCEP Climate Forecast System. Journal of Climate, 19(15): 3483–3517, doi: 10.1175/JCLI3812.1
Saji N H, Goswami B N, Vinayachandran P N, et al. 1999. A dipole mode in the tropical Indian Ocean. Nature, 401(6751): 360–363
Saji N H, Yamagata T. 2002. Structure of SST and surface wind variability during Indian Ocean Dipole mode events: COADS observations. Journal of Climate, 16(16): 2735–2751
Shi Li, Hendon H H, Alves O, et al. 2012. How predictable is the Indian Ocean Dipole?. Monthly Weather Review, 140(12): 3867–3884
Song Xunshu, Chen Dake, Tang Youmin, et al. 2018. An intermediate coupled model for the tropical ocean-atmosphere system. Science China: Earth Sciences, 61(12): 1859–1874, doi: 10.1007/s11430-018-9274-6
Tan Xiaoxiao, Tang Youmin, Lian Tao, et al. 2020. Effects of semistochastic westerly wind bursts on ENSO predictability. Geophysical Research Letters, 47(14): e2019GL086828
Tang Youmin, Kleeman R, Moore A M. 2004. SST Assimilation experiments in a tropical Pacific Ocean model. Journal of Physical Oceanography, 34(3): 623–642, doi: 10.1175/3518.1
Tang Youmin, Zhang Ronghua, Liu Ting, et al. 2018. Progress in ENSO prediction and predictability study. National Science Review, 5: 826–839, doi: 10.1093/nsr/nwy105
Trenberth K E. 1984. Some effects of finite sample size and persistence on meteorological statistics. Part I. Autocorrelations. Monthly Weather Review, 112(12): 2359–2368, doi: 10.1175/1520-0493(1984)112<2359:SEOFSS>2.0.CO;2
Vinayachandran P N, Francis P A, Rao S A. 2009. Indian Ocean Dipole: processes and impacts. In: Mukunda N, ed. Current Trends in Science. Bangalore, India: Indian Academy of Sciences, 569–589
Wajsowicz R C. 2005. Potential predictability of tropical Indian Ocean SST anomalies. Geophysical Research Letters, 32(24): L24702, doi: 10.1029/2005GL024169
Wajsowicz R C. 2007. Seasonal-to-interannual forecasting of tropical Indian Ocean sea surface temperature anomalies: Potential predictability and barriers. Journal of Climate, 20(13): 3320–3343, doi: 10.1175/JCLI4162.1
Wang Huijun. 2002. The instability of the East Asian summer monsoon–ENSO relations. Advances in Atmospheric Sciences, 19(1): 1–11, doi: 10.1007/s00376-002-0029-5
Wu Tongwen, Song Lianchun, Li Weiping, et al. 2014. An overview of BCC climate system model development and application for climate change studies. Journal of Meteorological Research, 28(1): 34–56
Wu Yanling, Tang Youmin. 2019. Seasonal predictability of the tropical Indian Ocean SST in the North American multimodel ensemble. Climate Dynamics, 53(5): 3361–3372
Xiao Mingzhong, Zhang Qiang, Singh V P. 2015. Influences of ENSO, NAO, IOD and PDO on seasonal precipitation regimes in the Yangtze River Basin, China. International Journal of Climatology, 35(12): 3556–3567, doi: 10.1002/joc.4228
Xie Shangping, Hu Kaiming, Hafner J, et al. 2009. Indian Ocean capacitor effect on Indo-Western Pacific climate during the summer following El Niño. Journal of Climate, 22(3): 730–747, doi: 10.1175/2008JCLI2544.1
Zhang Shouwen, Song Chunyang, Wang Hui, et al. 2018. Evaluation of the hindcasting main SSTA modes of the global key regions based on the CESM forecasting system. Haiyang Xuebao (in Chinese), 40(9): 18–30
Zhang Qiang, Xu Chongyu, Jiang Tong, et al. 2007. Possible influence of ENSO on annual maximum streamflow of the Yangtze River, China. Journal of Hydrology, 333(2–4): 265–274
Zhang Ronghua, Zebiak S E, Kleeman R, et al. 2005. Retrospective El Niño forecasts using an improved intermediate coupled model. Monthly Weather Review, 133(9): 2777–2802, doi: 10.1175/MWR3000.1
Zhao Mei, Hendon H H. 2009. Representation and prediction of the Indian Ocean Dipole in the POAMA seasonal forecast model. Quarterly Journal of the Royal Meteorological Society, 135(639): 337–352, doi: 10.1002/qj.370
Zheng Fei, Fang Xianghui, Zhu Jiang, et al. 2016. Modulation of Bjerknes feedback on the decadal variations in ENSO predictability. Geophysical Research Letters, 43(24): 12560–512568
Zheng Fei, Zhu Jiang, Zhang Ronghua, et al. 2006. Improved ENSO forecasts by assimilating sea surface temperature observations into an intermediate coupled model. Advances in Atmospheric Sciences, 23(4): 615–624, doi: 10.1007/s00376-006-0615-z